

Dependent scattering and fractal microstructure determine the transparency of aerogel monoliths

Cite as: APL Photon. 10, 046103 (2025); doi: 10.1063/5.0238739

Submitted: 13 September 2024 • Accepted: 4 March 2025 •

Published Online: 4 April 2025



View Online



Export Citation



CrossMark

Refet A. Yalcin,¹ Patricia E. McNeil,² Abhinav Bhanawat,¹ Ricardo Martinez,¹
Clareh N. Kashanchi,³ Sarah H. Tolbert,^{2,3,4} Bruce S. Dunn,^{2,4} and Laurent Pilon^{1,4,5,a)}

AFFILIATIONS

¹Mechanical and Aerospace Engineering Department, University of California, Los Angeles, Los Angeles, California 90095-1597, USA

²Material Science and Engineering Department, University of California, Los Angeles, Los Angeles, California 90095-1595, USA

³Department of Chemistry & Biochemistry, University of California, Los Angeles, Los Angeles, California 90095-1597, USA

⁴California NanoSystems Institute, University of California, Los Angeles, Los Angeles, California 90095, USA

⁵Institute of the Environment and Sustainability, University of California, Los Angeles, Los Angeles, California 90095, USA

^{a)}Author to whom correspondence should be addressed: pilon@seas.ucla.edu

ABSTRACT

This study reveals how dependent scattering and microstructure significantly affect electromagnetic wave propagation through aerogel monoliths, contributing to their transparency. Light scattering by particle ensembles is considered “dependent” when the scattering properties rely not only on particle size and optical constants but also on their spatial distribution, typically occurring when the average interparticle distance is small in comparison with the wavelength of incident radiation. Addressing dependent scattering requires solving Maxwell’s equations for complex heterogeneous structures, which is computationally demanding and usually limited to sample thicknesses on the same scale as the wavelength. This study combines computer-generated ambigels of fractal aggregates of polydisperse nanoparticles and the radiative transfer with reciprocal transaction method to predict the transmittance of thick ambigel slabs. Transmittance measurements of ambiently dried aerogel monoliths (ambigels) with porosities from about 50% to 90% closely matched the predicted values for their digital twins. However, ignoring dependent scattering or particle aggregation led to inaccurate predictions. This study validated the computational framework, and its findings offer insights for designing photonic metamaterials and analyzing their interactions with electromagnetic waves.

© 2025 Author(s). All article content, except where otherwise noted, is licensed under a Creative Commons Attribution-NonCommercial-NoDeriv 4.0 International (CC BY-NC-ND) license (<https://creativecommons.org/licenses/by-nc-nd/4.0/>). <https://doi.org/10.1063/5.0238739>

NOMENCLATURE

D_f	fractal dimension	n_m	continuous medium refractive index
d_p	pore size (nm)	N	number of particle ensembles
$f(r_s)$ or $f(d_p)$	particle or pore size distributions	N_s	number of particles in a particle ensemble
f_v	particle volume fraction	N_T	number of particles per unit volume (m^{-3})
h_{vis}	visible haze	N_{cl}	number of clusters in the computational domain (m^{-3})
I_λ	spectral radiation intensity ($\text{W m}^{-2} \text{sr}^{-1} \text{nm}^{-1}$)	P	pressure (Pa)
k_s	particle absorption index	P_0	saturation vapor pressure (Pa)
L	aerogel slab thickness (mm)	Q_{abs}	absorption efficiency factor
m	relative particle complex index of refraction, $m = m_s/n_m$	Q_{sca}	scattering efficiency factor
m_s	particle complex index of refraction, $m_s = n_s + ik_s$	R_c	radius of spherical particle ensemble
n_s	particle refractive index	\mathbf{r}	location vector (m)
		r_s	particle radius (nm)
		\bar{r}_s	average particle radius (nm)

\mathbf{s}	direction vector
\mathbf{T}^{ic}	incoherent T-matrix
\mathbf{T}^c	coherent T-matrix
T_{nh}	normal-hemispherical transmittance
V_e	volume of particle ensemble (nm ³)
w	volume of gas adsorbed gas per unit mass of aerogels (cm ³ g ⁻¹)
x_s	particle size parameter, $x_s = 2\pi r_s/\lambda$

Greek Symbols

β	effective extinction coefficient (m ⁻¹)
θ	polar angle (rad)
κ	effective absorption coefficient (m ⁻¹)
λ	wavelength in vacuum (nm)
σ	standard deviation of particle radius r_s (nm)
σ_s	effective scattering coefficient (m ⁻¹)
ϕ	aerogel porosity, $\phi = 1 - f_v$
Φ_T	effective scattering phase function
φ	azimuthal angle (rad)
χ_s	size parameter, $\chi_s = 2\pi r_s/\lambda$
Ω	solid angle (sr)

Subscripts

λ	spectral value
i	incident radiation
j	j th particle ensemble ($1 \leq j \leq N$)
r	reflected radiation
t	transmitted radiation

Superscripts

c	coherent radiation
d	dependent scattering
ic	incoherent radiation
ind	independent scattering
M	Lorenz-Mie theory

I. INTRODUCTION

Porous materials such as polymeric foams and glass wools have been used extensively for thermal insulation applications. These materials are opaque and often white in appearance due to scattering by struts and fibers with sizes larger than the wavelength of light. However, several applications such as windows,^{1,2} skylights,³ and solar thermal energy conversion systems⁴ require materials that are optically transparent to incident light but are thermally insulating for reducing heat loss. For such applications, aerogel monoliths are highly promising candidates provided that they can be made transparent and not translucent.

Aerogels are mesoporous materials consisting of fractal aggregates of particles with diameters spanning from 1 to 10 nm and small pore sizes between 2 and 50 nm. In addition, they possess a large specific surface area, a porosity greater than 70%, low thermal conductivity comparable to that of air, and a low effective refractive index. Their thermal conductivity typically decreases with increasing porosity achieved by increasing pore size and thus

light scattering. The increase in light scattering renders the material hazy and decreases the optical clarity of aerogel monoliths. In fact, highly insulating aerogels with porosity exceeding 95% exhibit a translucent quality rather than transparency and possess a blue tint. Synthesizing aerogels that are both thermally insulating and optically transparent is challenging and requires optimizing the porosity and microstructure to reduce electromagnetic (EM) wave scattering.

Light transfer simulations usually treat aerogels as homogeneous with some effective absorption and scattering coefficients determined by assuming that the constituent particles scatter light independently of one another.⁵ However, this may not hold true for aerogel monoliths with relatively large particle volume fractions or low porosities. Indeed, light transfer through aerogels not only depends on the primary particle size, particle volume fraction, and optical constants of its constituent particles but may also depend on their spatial arrangement. This phenomenon has been termed “dependent scattering,” which usually occurs when the average interparticle distance is small compared to the wavelength of incident light.⁶ Simulating light transfer through aerogel monoliths is complicated because of the difficulty in generating realistic and representative complex microstructures.

The present study aims to understand the interaction of aerogel monoliths with EM waves and the effect of their microstructures. First, a computational framework was developed for simulating EM wave transport through realistic computer-generated plane-parallel thick silica aerogel monoliths and accounting for their heterogeneous and fractal microstructures. The simulations of radiation transfer accounted for dependent scattering, coherent backscattering, and near-field effects in the aerogel microstructure. Finally, ambiently dried aerogel (ambigel) monoliths with porosity spanning from 50% to 90% were synthesized and characterized. Their normal-hemispherical spectral transmittance was measured experimentally and compared with the solutions of the radiative transfer equation assuming independent scattering or accounting for dependent scattering and the fractal aerogel microstructures.

II. BACKGROUND

A. Maxwell's equations

The transport of electromagnetic waves in heterogeneous structures, such as particle suspensions or solid mesoporous slabs, is governed by Maxwell's equations. Typically, these equations are solved through numerical methods, such as the finite difference time domain (FDTD),⁷ discrete dipole approximation (DDA),⁸ finite element method (FEM),⁹ and superposition T-matrix¹⁰ methods, for example. In fact, such techniques have been used to investigate light scattering by particles consisting of a relatively limited number of fractally aggregated particles of dust, ice, and silica.^{11–13} However, when the dimensions of the heterogeneous medium are large and the particles are small relative to the wavelength of the incident radiation, solving Maxwell's equations becomes challenging due to the high computational demands of these methods. This is the case of millimeter thick plane-parallel aerogel slabs consisting of fractally aggregated nanoparticles. Then, an alternative approach is using radiation transfer theory, which involves solving the radiative transfer equation (RTE) and treating the heterogeneous medium as a homogeneous structure with effective radiative properties.¹⁴

B. Radiative transfer equation

The local spectral radiation intensity field $I_\lambda(\mathbf{r}, \hat{s})$ at a given location \mathbf{r} and propagating in direction \hat{s} within a heterogeneous medium can be predicted by solving the non-emitting, absorbing, and scattering radiative transfer equation (RTE) expressed as¹⁵

$$\frac{dI_\lambda(\mathbf{r}, \hat{s})}{ds} = -(\sigma_{s,\lambda} + \kappa_\lambda)I_\lambda(\mathbf{r}, \hat{s}) + \frac{\sigma_{s,\lambda}}{4\pi} \int_{4\pi} I_\lambda(\mathbf{r}, \hat{s}') \Phi_{T,\lambda}(\hat{s}', \hat{s}) d\Omega'. \quad (1)$$

Here, $\sigma_{s,\lambda}$ and κ_λ are the heterogeneous medium effective scattering coefficient and absorption coefficient, respectively, while $\Phi_{T,\lambda}(\hat{s}', \hat{s})$ is the effective scattering phase function. The RTE accounts for the extinction of the intensity due to out-scattering and absorption as well as its amplification due to in-scattering and multiple scattering from direction \hat{s}' into direction of interest \hat{s} . The RTE is numerically solved to predict the local radiation intensity $I_\lambda(\mathbf{r}, \hat{s})$ along various directions for given effective radiation characteristics κ_λ , $\sigma_{s,\lambda}$, and $\Phi_{T,\lambda}(\hat{s}', \hat{s})$ at wavelength λ .

C. Independent scattering

Mishchenko¹¹ derived the Radiative Transfer Equation (RTE) from Maxwell's equations by assuming that (i) the positions of the particles are independent of one another, (ii) the medium has a sufficiently high concentration of particles, and (iii) the average distance between particles far exceeds the wavelength of the incident radiation. Given these conditions, a particle's scattering is unaffected by nearby particles, enabling the calculation of effective absorption and scattering coefficients of the particle ensemble using superposition principles. This involves summing the absorption and scattering cross sections of each individual particle in the suspension and dividing by the corresponding total volume; this scenario is referred to as "independent scattering." The effective radiative properties κ_λ^{ind} , $\sigma_{s,\lambda}^{ind}$, and $\Phi_{T,\lambda}(\hat{s}', \hat{s})$ for a heterogeneous medium composed of monodisperse spherical particles of radius r_s and complex refractive index $m_{s,\lambda} = n_{s,\lambda} + ik_{s,\lambda}$ within a non-absorbing medium of refractive index $n_{m,\lambda}$ can be described as¹⁵

$$\sigma_{s,\lambda}^{ind} = N_T \pi r_s^2 Q_{sca,\lambda}^M(\chi_s, m_\lambda) \quad \text{and} \quad \kappa_\lambda^{ind} = N_T \pi r_s^2 Q_{abs,\lambda}^M(\chi_s, m_\lambda), \quad (2)$$

$$\Phi_{T,\lambda}(\hat{s}', \hat{s}) = \Phi_\lambda^M(\hat{s}', \hat{s}). \quad (3)$$

In this context, $\chi_s = 2\pi r_s/\lambda$ represents the particle size parameter, and $m_\lambda = m_{s,\lambda}/n_{m,\lambda}$ is the particle's relative complex refractive index. In addition, $N_T = 3f_v/4\pi r_s^3$ denotes the number of particles per unit volume of the medium, with f_v being the particle volume fraction. The absorption efficiency factor $Q_{abs,\lambda}^M(\chi_s, m_\lambda)$, the scattering efficiency factor $Q_{sca,\lambda}^M(\chi_s, m_\lambda)$, and the scattering phase function $\Phi_\lambda^M(\hat{s}', \hat{s})$ for a single spherical particle can be estimated using the Lorenz–Mie theory.¹⁶ Analogous expressions are available for heterogeneous media containing polydisperse spherical particles with varying size distributions.¹⁵

D. Dependent scattering

As the particle volume fraction in a suspension or a monolith increases, the interparticle distance becomes similar or smaller than the wavelength λ of the incident light, causing particles to

scatter in a dependent manner rather than independently.⁶ Dependent scattering effects include the far-field interference of scattered waves as well as near-field interactions.⁶ Tien and Drolen¹⁷ reviewed various analytical models accounting for dependent scattering in packed fluidized beds developed prior to 1987,^{18–21} proposing a scattering regime map based on size parameter χ_s and particle volume fraction f_v under the assumption of an orthorhombic particle arrangement. However, recent work has shown that radiation characteristics depend on the specific spatial distribution of particles, suggesting that orthorhombic packing and other standardized packings may not accurately represent particle suspensions or aggregates where dependent scattering is dominant. Instead, the scattering efficiency factor and asymmetry factor for a group of particles can be described as $Q_{sca,\lambda}^d(\chi_s, m_\lambda, \bar{d}/\lambda)$ and $g_\lambda^d(\chi_s, m_\lambda, \bar{d}/\lambda)$, respectively, where \bar{d} is the average interparticle distance. A new regime map was proposed to replace that of Tien and Drolen¹⁷ to better distinguish dependent and independent scattering regimes using χ_s vs \bar{d}/λ , reflecting these advances.²²

A common method for addressing dependent scattering involves the use of the static structure factor, which represents the spatial correlation between a given particle and its immediate neighbors.^{23,24} This factor is applied so as to multiplicatively alter the independent scattering solution.²⁴ For instance, Tsang and Ishimaru²⁵ formulated the dense medium radiative transfer (DMRT) theory from the second moment equations of electromagnetic wave theory, separating the scattered field into coherent and incoherent components. The incoherent scattered field complies to the Bethe–Salpeter equation²⁵ under the quasi-crystalline approximation with coherent potential. In essence, the DMRT method handles dependent scattering by adjusting the scattering coefficient and asymmetry parameter predicted from the independent scattering assumption with a multiplicative introduction of the static structure factor. However, it should be recognized that the DMRT method does not consider near-field effects or particle aggregation.²⁶

E. Radiative transfer with reciprocal transaction (R^2T^2) method

Muinonen *et al.*²⁷ and Väisänen *et al.*²⁸ introduced the Radiative Transfer with Reciprocal Transactions (R^2T^2) method to solve the Radiative Transfer Equation (RTE) in semi-infinite media using the Monte Carlo approach. Initially, the R^2T^2 method utilizes the T-matrix method to determine the effective radiation characteristics of dense particle suspensions as opposed to using the Lorenz–Mie theory. This technique accounts for both far-field and near-field effects in computing the scattered electric field. In practical terms, a significant number (>500) of sufficiently large spherical particle ensembles is generated (see Fig. S4 of the [supplementary material](#)) and sampled so as to ensure an ergodic medium, and the T-matrix T of the particle ensemble is computed. However, the computed T-matrix T cannot be directly applied since it treats the electromagnetic radiation as incoming from free space onto the particle ensemble. In aerogel monoliths, light only undergoes volumetric scattering by the particles, matching the incoherent component of the T-matrix,²⁶ without encountering artificial surface boundaries associated with the coherent component of the T-matrix. Therefore, the incoherent T-matrix T^{ic} should be used exclusively when evaluating the

radiative properties of the particle ensemble. To do so, the coherent T-matrix T^c can be obtained by an arithmetic average of all “ j ” particle ensemble ($1 \leq j \leq N$) T-matrices according to Ref. 28,

$$T^c = \lim_{N \rightarrow \infty} \frac{1}{N} \sum_{j=1}^N T_j. \quad (4)$$

Then, the incoherent T-matrix of particle ensemble “ j ” of T-matrix T_j is given by $T_j^{ic} = T_j - T^c$. Details of the method applied to the plane-parallel slabs of heterogeneous media were presented in our previous study and need not be repeated.²⁶

The traditional Monte Carlo method assumes independent scattering, and the incident electromagnetic field on any particle is treated as a plane wave, with the Mueller matrix used to determine the scattering direction. Conversely, the R^2T^2 method accounts for radiation incident on a particle ensemble by using the outward scattered radiation by the ensemble at the previous scattering event. At each scattering event, the method uses the scattering characteristics of a randomly chosen particle ensemble from the previously generated N ensembles. This approach aligns the R^2T^2 method more closely with solving Maxwell’s equations, contrasting with the traditional methods typically used to solve the Radiative Transfer Equation (RTE).

The aim of this study is to evaluate and quantify the impact of particle aggregation and dependent scattering on electromagnetic wave propagation through silica aerogels. A computational approach based on the R^2T^2 method was designed to predict the radiation intensity field in realistic, computer-generated plane-parallel aerogel monoliths of different thicknesses. This method effectively captures multiple scattering as well as dependent scattering and near-field effects within the fractal aggregates of nanoparticles making up the aerogels. This study examined the validity of the independent scattering approximation and explored how particle volume fraction, size distribution, and spatial arrangement affect aerogel interaction with electromagnetic waves. The synthesized ambigels were also characterized, and their normal-hemispherical transmittance measurements were compared with predictions for their digital twins. The framework established in this study offers valuable potential in the development of mesoporous thin films or slabs and other photonic metamaterials.

III. ANALYSIS

A. Problem statement

Figure 1 depicts the scattering of light within an aerogel monolith and highlights the different length scales of the problem. Let us consider a mesoporous aerogel of thickness L characterized by a spherical particle size distribution $f(r_s)$ with a porosity ϕ , a fractal dimension D_f , and a pore size distribution $f(d_p)$. The silica nanoparticles had a complex refractive index $m_{s,\lambda} = n_{s,\lambda} + ik_{s,\lambda}$, while the continuous medium was air and non-absorbing with refractive index $n_{m,\lambda}$ at a given wavelength λ .

B. Computer-generated aerogels

The so-called diffusion-limited cluster-cluster aggregation (DLCCA) method was employed to generate fractal mesoporous slabs composed of polydisperse spherical particles.^{29,30} To do so,

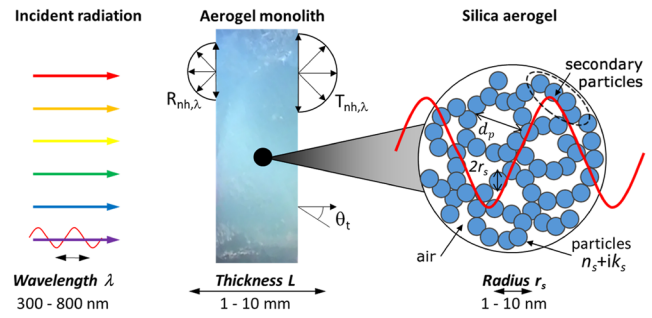


FIG. 1. Schematic of an aerogel monolith of thickness L constituting primary particles of radius r_s and pore size d_p subjected to incident light of wavelength λ .

the DLCCA method first generated a suspension of randomly distributed monodisperse or polydisperse particles such that the number of clusters N_{cl} equaled the number of particles. Then, the DLCCA mechanism was used to simulate the aggregation of particles into clusters and the subsequent merging of smaller clusters into larger ones with fractal dimension D_f matching the measured value for a specific sample and used as an input parameter in the DLCCA method.²⁹ Here, hundreds of particle ensembles were generated in a relatively short amount of time via parallelization of the code developed by Morán *et al.*³⁰ The computer generation of aerogels was completed when $N_{cl} = 1$ corresponding to the situation where all particles were in contact with one another in a single cluster.

A total of $N = 512$ aerogels were generated inside cubic computational domains using the DLCCA method for a given particle volume fraction f_v and size distribution $f(r_s)$. Then, spherical particle ensembles of radius R_e were cropped from the center of the $N = 512$ cubic domains. To establish statistically representative mesoporous structures when the pore size becomes larger than the particles and contributes to scattering, the spherical particle ensembles radius was taken as $R_e = 5 \times \max(r_s, d_p/2)$. This choice of R_e ensured that the spherical particle ensembles were sufficiently large and ergodicity was achieved for the highest porosities and accurately captured scattering by pores.

C. Light transfer simulations

Solutions of the RTE in mesoporous slabs were predicted numerically using the Monte Carlo method assuming independent scattering.³¹ The effective scattering phase function, absorption coefficient, and scattering coefficient were computed using the Lorenz-Mie theory and Eqs. (2) and (3) for monodisperse spherical particles of arbitrary radius r_s and porosity $\phi = 1 - f_v$. Solutions of the RTE were formulated in relation to the spectral normal-hemispherical transmittance $T_{nh,\lambda}$ and reflectance $R_{nh,\lambda}$ given by

$$T_{nh,\lambda} = \frac{\int_0^{2\pi} \int_0^{\pi/2} I_{\lambda,t}(L, \theta_t, \varphi_t) \cos \theta_t \sin \theta_t d\theta_t d\varphi_t}{I_{\lambda,i} \Delta \Omega_i}, \quad (5)$$

$$R_{nh,\lambda} = \frac{\int_0^{2\pi} \int_0^{\pi/2} I_{\lambda,r}(0, \theta_r, \varphi_r) \cos \theta_r \sin \theta_r d\theta_r d\varphi_r}{I_{\lambda,i} \Delta \Omega_i}, \quad (6)$$

where θ_t and φ_t are, respectively, the polar and azimuthal angles of the transmitted intensity $I_{\lambda,t}$, θ_r and φ_r are the corresponding angles of the reflected intensity $I_{\lambda,r}$, while $I_{\lambda,i}$ is the intensity normally incident onto the slab in solid angle Ω_i . Note that, when assuming independent scattering, the solution of the RTE only depends on the particles' size distribution and volume fraction, not on their spatial arrangement.¹⁵

The R^2T^2 method accounting for dependent scattering effects in plane-parallel slabs, detailed in Ref. 28, was utilized in this work. This implementation employed N spherical particle ensembles generated by the DLCCA algorithm to represent aerogel structures. In addition, the haze of aerogel slabs is the fraction of visible light intensity that is scattered and transmitted at angles greater than 2.5° from normal according to the ASTM D1003 standard and can be defined as⁵

$$h_{vis} = 1 - \frac{\int_0^{360^\circ} \int_0^{2.5^\circ} \int_{380\text{ nm}}^{780\text{ nm}} P_\lambda I_{\lambda,t}(L, \theta_t, \varphi_t) \cos \theta_t \sin \theta_t d\lambda d\theta_t d\varphi_t}{\int_0^{360^\circ} \int_0^{90^\circ} \int_{380\text{ nm}}^{780\text{ nm}} P_\lambda I_{\lambda,t}(L, \theta_t, \varphi_t) \cos \theta_t \sin \theta_t d\lambda d\theta_t d\varphi_t}, \quad (7)$$

where P_λ is the so-called photopic spectral luminous efficiency function of the human eye.³² Haze is used to evaluate whether slabs are transparent or translucent, i.e., a perfectly transparent slab would have $h_{vis} = 0$.

IV. MATERIALS AND METHODS

A. Aerogel synthesis

Mesoporous monoliths based on silica were synthesized via a sol-gel method catalyzed by acid and base.² Tetraethyl orthosilicate (TEOS), methyltriethoxysilane (MTES), ethanol, formamide, and water were mixed with respective molar ratios of 1.5:1:6.25:5:6.25. Then, a 2M NH_4OH base-catalyst was incorporated at a base-to-sol volume ratio of 6:17. Next, the sol was promptly moved into a $10 \times 10 \times 0.15\text{ cm}^3$ plastic cartridge, where the sol underwent gelation within a few minutes. The cassette was then aged for two days at room temperature, and the gel monoliths were extracted from the molds and submerged in ethanol. Moreover, the submerging ethanol was then replaced with heptane, so as to minimize capillary stress during drying thanks to its lower surface tension. Finally, the aerogels were ambiently dried by heptane drainage, allowing the pore solvent to evaporate slowly in an air-tight vessel over the span of seven days.

Three different samples with varying microstructures were synthesized using the aforementioned method with some variations. During the solvent exchange step, sample 1 underwent a surface modification treatment consisting of immersing the sample in a solution of a 1 vol. % of trimethylchlorosilane (TMCS) in heptane for 30 min, resulting in a hydrophobic surface. This sample was rinsed in ethanol to eliminate secondary substances produced by the chlorosilane reaction with silica. The ethanol was subsequently exchanged with heptane and dried in a high heptane concentration atmosphere. This treatment effectively minimized capillary tension during the drying phase, ensuring that the slab retained a porosity of near 90%.² Moreover, samples 2 and 3 did not undergo a TMCS treatment and thus had significantly lower porosities in comparison with sample 1. Finally, samples 1 and 2 underwent a calcination process for 5 h, while sample 3 underwent a calcination process for 24 h at 500°C in static air to eliminate any organic phase.

B. Microstructure characterization

Low-temperature nitrogen adsorption porosimetry measurements were performed using an accelerated surface area and porosity analyzer ASAP 2020 Plus (Micromeritics Instrument Corp., Norcross, GA). The specific surface area, micropore and mesopore volumes, pore size distribution, and volume fraction of open porosity were computed following the methods detailed in Ref. 33. Nitrogen porosimetry isotherms were utilized to calculate the surface fractal dimension D_f via the Frenkel-Halsey-Hill method based on the following expression³⁴

$$\ln w = C - (3 - D_f) \ln \left(RT \ln \frac{P_0}{P} \right), \quad (8)$$

where w is the adsorbed volume of nitrogen gas per unit mass of aerogels (in $\text{cm}^3\text{ STP g}^{-1}$). Here also, T denotes the temperature, while P and P_0 are the pressure and saturation vapor pressure, respectively. In addition, R is the ideal gas constant, while C is an empirical constant. Finally, the transmission electron microscopy (TEM) images of sample powder were captured using a FEI Tecnai G2 T20 electron microscope. The images were used to determine the average silica particle size.

C. Transmittance measurements

Measurements of the spectral normal-hemispherical transmittance $T_{nh,\lambda}$ of the synthesized aerogels were taken using a double-beam ultraviolet-visible (UV-Vis) spectrophotometer (iS50, Thermo Fisher Scientific, USA) equipped with an integrating sphere (EVO220, Thermo Fisher Scientific, USA). Here, laboratory measurements of transmittance were obtained for wavelength λ spanning from 350 to 800 nm, in increments of 1 nm. Here, a baseline transmittance measurement was performed with air such that its corresponding normal-hemispherical transmittance $T_{nh,\lambda}$ was 100%.

V. RESULTS AND DISCUSSION

A. Material characterization

Figure 2 shows (a) a TEM image and (b) a photograph of ambigel sample 1. The TEM images indicate that the silica particles

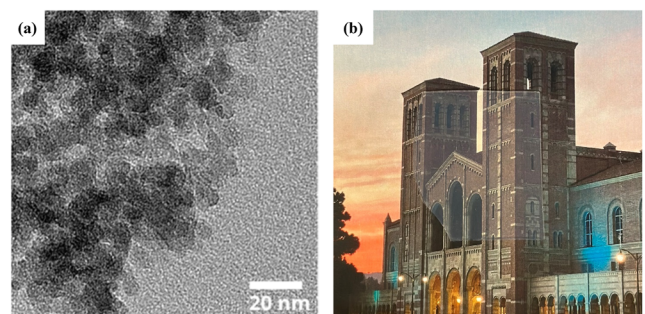


FIG. 2. (a) TEM image and (b) photograph of synthesized transparent ambigel sample 1 sitting on a printed image of UCLA Royce Hall.

TABLE I. Synthesis method, particle size $\bar{r}_s \pm \sigma$, porosity ϕ , thickness L , and fractal dimensions D_f of the synthesized ambigel monoliths.²

Aerogel sample #	Synthesis method	Porosity, $\phi = 1 - f_v$ (%)	Thickness, L (mm)	Particle size, $\bar{r}_s \pm \sigma$ (nm)	Fractal dimension, D_f
1	TEOS, 1 vol. % TMCS, calcined	90.8	1.15	4.3 ± 1.0	2.4
2	TEOS, calcined 5 h	76.4	0.87	4.3 ± 1.0	2.4
3	TEOS, calcined 24 h	47.6	0.52	8.9 ± 2.5	2.6

for samples 1, 2, and 3 had an average radius \bar{r}_s and a standard deviation σ of $\bar{r}_s \pm \sigma$ of 4.3 ± 1.0 nm, 4.3 ± 1.0 nm, and 8.9 ± 2.5 nm, respectively.

Table I summarizes the microstructural parameters measured for samples 1, 2, and 3, including their porosity ϕ , particle radius $\bar{r}_s \pm \sigma$, and fractal dimension D_f . The sample porosity ϕ ranged from 90.8% for sample 1 to 47.6% for sample 3.

B. Characterization of computer-generated aerogels

Figures 3(a)–3(c) illustrate the computer-generated particle ensembles representative of samples 1–3, respectively, described in Table I. Figure 3(d) illustrates a particle ensemble having the same porosity, fractal dimension, and average particle radius as sample 1 but with monodisperse particles. Finally, Figs. 3(e)–3(h) illustrate spherical particle ensembles of radii $R_e = 75, 30, 50,$ and 75 nm, respectively, that were cropped from Figs. 3(a)–3(d). It should be noted that each of the 512 cropped ensembles contains ~ 70 – 500 particles, thereby maintaining a meaningfully defined fractal dimension³⁵ and matching that of the larger aggregates generated by the DLCCA method. This is confirmed both geometrically and optically by the convergence of pore size distribution and scattering coefficient with the increasing ensemble radius (see Fig. S4 of the [supplementary material](#)). The data that contain spatial coordinates and radii of particles are publicly available for all samples.³⁶

Figure 4 shows (a) the pore size distribution $f(d_p)$ and (b) the cumulative pore size distribution function (CDF) of sample 1 and of a representative aerogel structure digitally generated using DLCCA with polydisperse particles of radius $r_s = 4.3 \pm 1$ nm and particle volume fraction $f_v = 9.2\%$, i.e., porosity $\phi = 90.8\%$ [Fig. 3(a)]. The pore size distribution $f(d_p)$ was calculated using the method we previously developed.²⁹ Figure 4 indicates that when the same imposed porosity $\phi = 90.8\%$ and fractal dimension $D_f = 2.4$ was used, the computer-generated structures using the DLCCA method had a tight pore size distribution $f(d_p)$ similar to that of sample 1 and yielded a peak pore size of ~ 25 nm. Similar results were obtained for samples 2 and 3 and their digital twins (see Fig. S2 of the [supplementary material](#)). Overall, these findings validate that the digitally generated aerogels were representative of the synthesized samples with a similar microstructure, including porosity, pore size distribution, and fractal dimension reported in Table I. It should also be noted that the predictions of light transfer through complex heterogeneous materials exhibiting anomalous diffusion such as Lévy glasses³⁷ using the R^2T^2 method have not been explored and fall outside the scope of this study.

C. Comparison of the independent scattering approximation and R^2T^2 methods

Figure 5 shows the normal-hemispherical transmittance $T_{nh,\lambda}$ of 1 mm-thick plane-parallel computer-generated aerogel monoliths consisting of aggregated monodisperse spherical particles of radius $r_s = 5$ nm, fractal dimension $D_f = 2.4$, and porosity ϕ equal to (a) 95%, (b) 90%, (c) 80%, and (d) 65% predicted by the R^2T^2 method. Figure 5 also shows the spectral transmittance $T_{nh,\lambda}$ predicted for the case of a suspension of randomly distributed spherical particles in vacuum with the same thickness, particle radius, and volume fraction as the aerogel slabs by solving the RTE (i) using the independent scattering assumption or (ii) accounting for dependent scattering using the R^2T^2 method.

Figure 5 indicates that the predictions accounting for dependent scattering for randomly distributed particles agreed well with those assuming independent scattering for large porosity $\phi = 95\%$. Here, the particle volume fraction was small and dependent scattering effects for randomly distributed particles were negligible. However, the transmittance of aerogel slabs predicted by accounting for the complex microstructure and dependent scattering was considerably lower compared to those considering randomly distributed particles with the same radius and particle volume fraction. This can be attributed to the fact that particle aggregation creates large structures in the form of chains of particles or secondary particles with characteristic size greater than individual particle size, thereby resulting in stronger scattering.

Notably, the transmittance of computer-generated aerogel slabs predicted by the R^2T^2 method increased with decreasing porosity ϕ , i.e., with increasing particle volume fraction f_v . In fact, for porosity $\phi = 65\%$, the predictions converged to those by the R^2T^2 method for randomly distributed particles for all wavelengths. This can be attributed to the fact that the interparticle distance for either aggregated or randomly distributed particles converged as the volume fraction of particles increased (see Fig. S1 of the [supplementary material](#)).

Overall, Fig. 5 establishes that accurate predictions of the transmittance $T_{nh,\lambda}$ of aerogels should account not only for dependent scattering but also for particle aggregation, particularly at large porosities. In addition, assuming independent scattering was found to significantly overpredict the transmittance at large porosities ($\phi > 90\%$) and substantially underestimate it at small porosities ($\phi < 80\%$) compared to those predicted by the R^2T^2 method accounting for both dependent scattering and the aerogel microstructure. The results can be misinterpreted as increasing wavelength decreases the discrepancy between methods, but this decrease is due to reducing optical thickness at those wavelengths as this study investigates

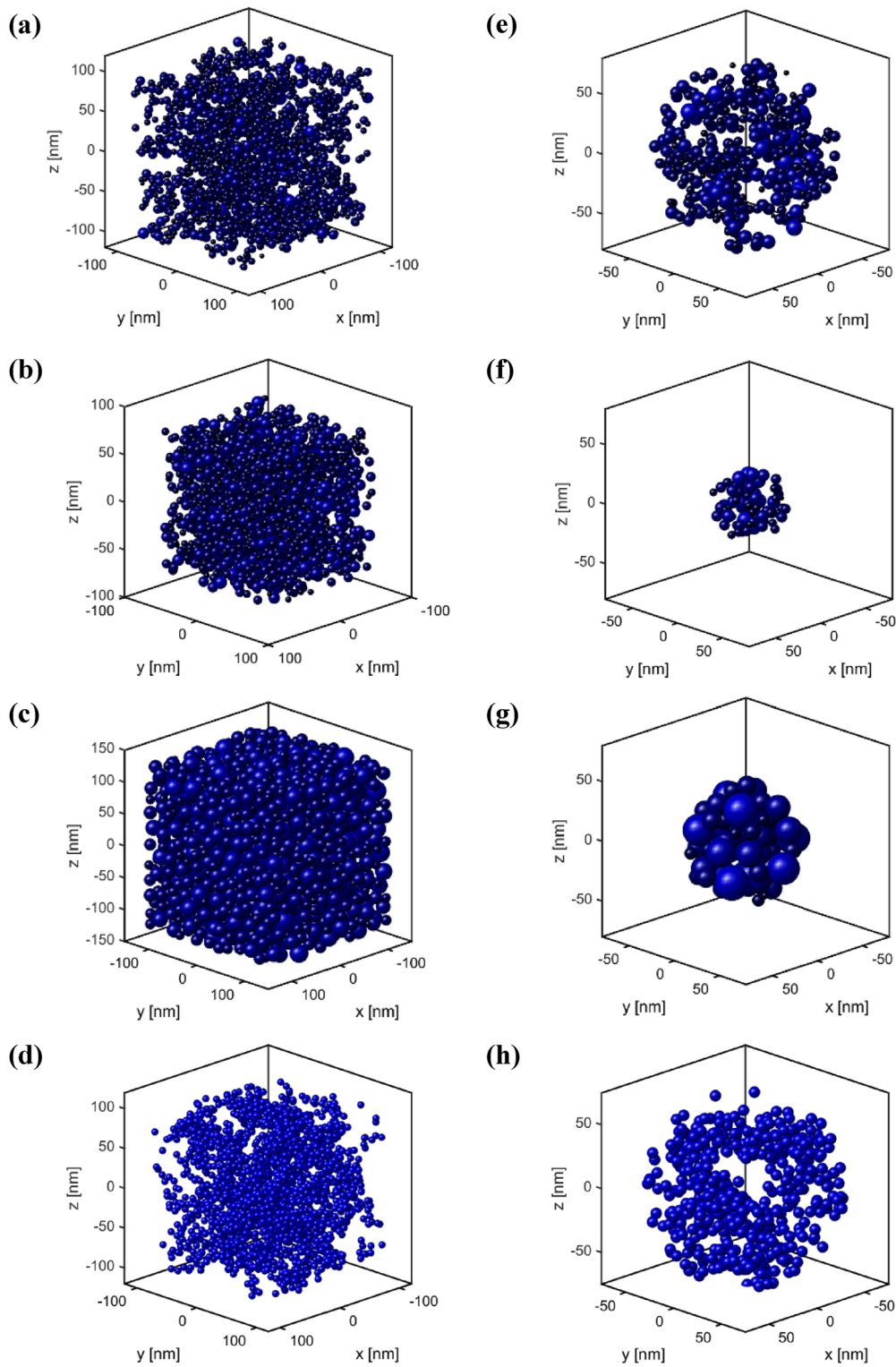


FIG. 3. (a)–(d) Computational domains populated by 2000 polydisperse spherical particles simulated with the DLCCA method for (a) $\phi = 90.8\%$, $\bar{r}_s \pm \sigma = 4.3 \pm 1.0$ nm; (b) $\phi = 76.4\%$, $\bar{r}_s \pm \sigma = 4.3 \pm 1.0$ nm; (c) $\phi = 47.6\%$, $\bar{r}_s \pm \sigma = 8.9 \pm 2.5$ nm; and (d) $\phi = 90.8\%$, $r_s = 4.3$ nm. (e)–(h) Computational domains cropped from (a)–(d), respectively.

11 April 2025 22:30:34

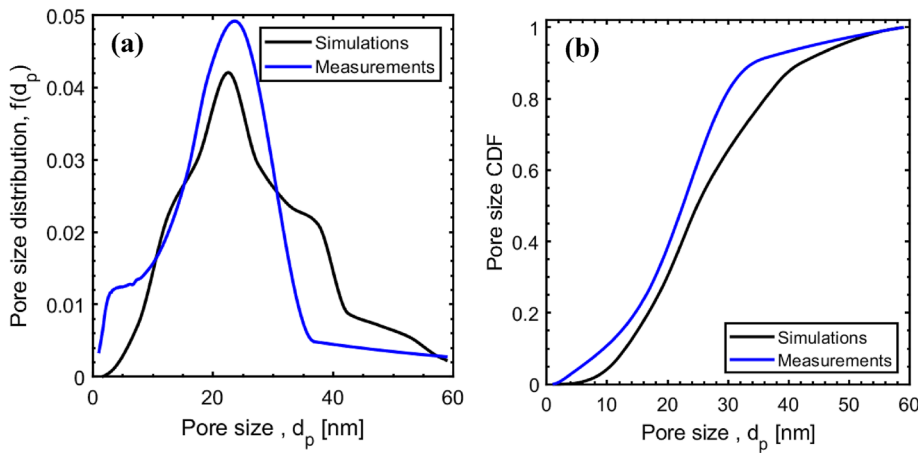


FIG. 4. (a) Pore size distributions and (b) cumulative distribution functions measured for sample 1 and computed for its digital twin generated using DLCCA with polydisperse particles of radius $\bar{r}_s \pm \sigma = 4.3 \pm 1$ nm and porosity $\phi = 90.8\%$.

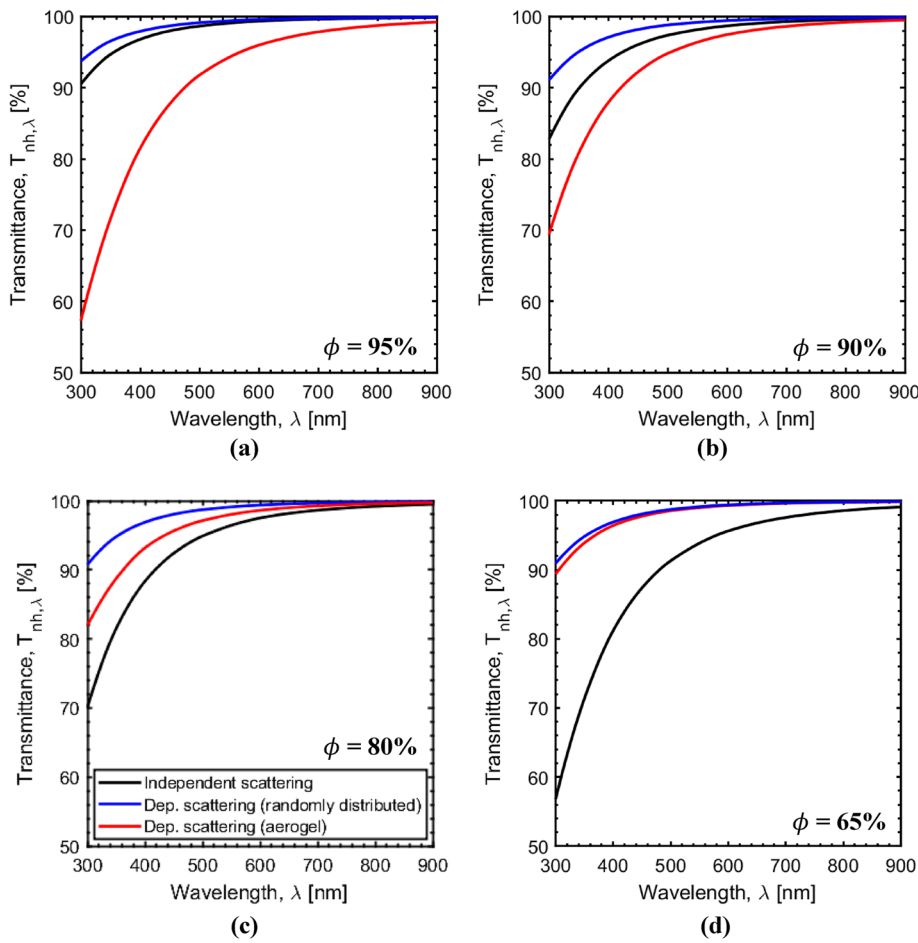


FIG. 5. Comparison of the aerogel monolith spectral normal-hemispherical transmittance $T_{nh,\lambda}$ with varying porosity ϕ equal to (a) 95%, (b) 90%, (c) 80%, and (d) 65% as a function of wavelength λ numerically predicted by the R^2T^2 method against the solutions of the RTE assuming independent scattering or accounting for dependent scattering by the R^2T^2 method but considering for a suspension consisting of randomly distributed particles. In all cases, $L = 1$ mm, $r_s = 5$ nm, $n_{s,\lambda} = 1.5$, $k_{s,\lambda} = 0$, $n_{m,\lambda} = 1$, and $k_{m,\lambda} = 0$.

haze and transmittance; however, Fig. S6 illustrates the log scale spectral normal hemispherical reflectances, which better show that the discrepancies between methods persist as the wavelength increases.

D. Effect of particle polydispersity

Figure 6(a) shows the normal-hemispherical transmittance $T_{nh,\lambda}$ computed by the R^2T^2 method for computer-generated

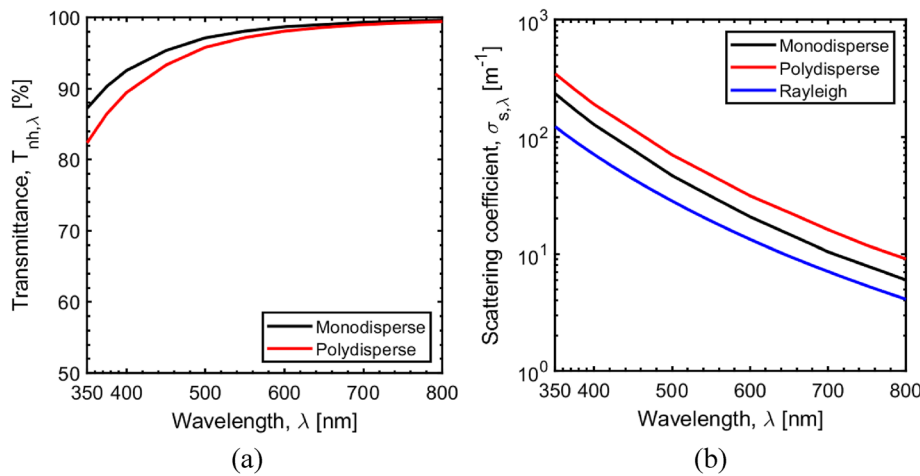


FIG. 6. Comparison of the spectral (a) normal-hemispherical transmittance $T_{nh,\lambda}$ and (b) scattering coefficient $\sigma_{s,\lambda}$ predicted by the R^2T^2 method for computer-generated aerogel monoliths consisting of monodisperse ($r_s = 4.3$ nm) or polydisperse ($\bar{r}_s \pm \sigma = 4.3 \pm 1.0$ nm) particles with $L = 1.15$ mm, $\phi = 90.8\%$, and $D_f = 2.4$, representative of sample 1. The scattering coefficient predicted by Eq. (2) assuming Rayleigh scattering for randomly distributed monodisperse particles of radius $r_s = 4.3$ nm is also shown for reference.

plane-parallel aerogel slabs representative of sample 1 with porosity $\phi = 90.8\%$, fractal dimension $D_f = 2.4$, and consisting of either polydisperse particles of normal distribution with $\bar{r}_s \pm \sigma = 4.3 \pm 1.0$ nm [Fig. 3(a)] or monodisperse particles with $r_s = 4.3$ nm [Fig. 3(d)]. Figure 6(b) shows the corresponding scattering coefficients $\sigma_{s,\lambda}$ averaged over the $N = 500$ particle ensembles generated in calculating $T_{nh,\lambda}$ reported in Fig. 6(a). It also shows the scattering coefficient predicted by Eq. (2), assuming Rayleigh scattering for randomly distributed monodisperse particles with the scattering efficiency factor $Q_{sca,\lambda} = 8/3\chi_s^4|m_\lambda^2 - 1|^2/|m_\lambda^2 + 1|^2$. Figure 6 indicates that particle polydispersity resulted in larger scattering and smaller transmittance in the visible. Figure S3(a) shows that polydispersity results in a larger pore size distribution compared to the monodisperse case for the same porosity and average particle size.

Therefore, a narrow particle size distribution is more desirable to minimize scattering and achieve transparent aerogel monoliths. In addition, Fig. 6(b) shows that the stronger scattering at shorter wavelengths predicted by Rayleigh scattering prevailed in aerogels, as commonly used to explain their blue tint. However, dependent scattering in the complex fractal microstructure enhanced scattering by nearly a factor of 1.5 compared with the predictions of Rayleigh scattering for randomly distributed monodisperse particles.

E. Visible haze

Figure 7(a) shows the visible haze h_{vis} of aerogels with a fractal dimension $D_f = 2.4$ computed by integrating over the visible wavelength according to Eq. (7) using the spectral directional

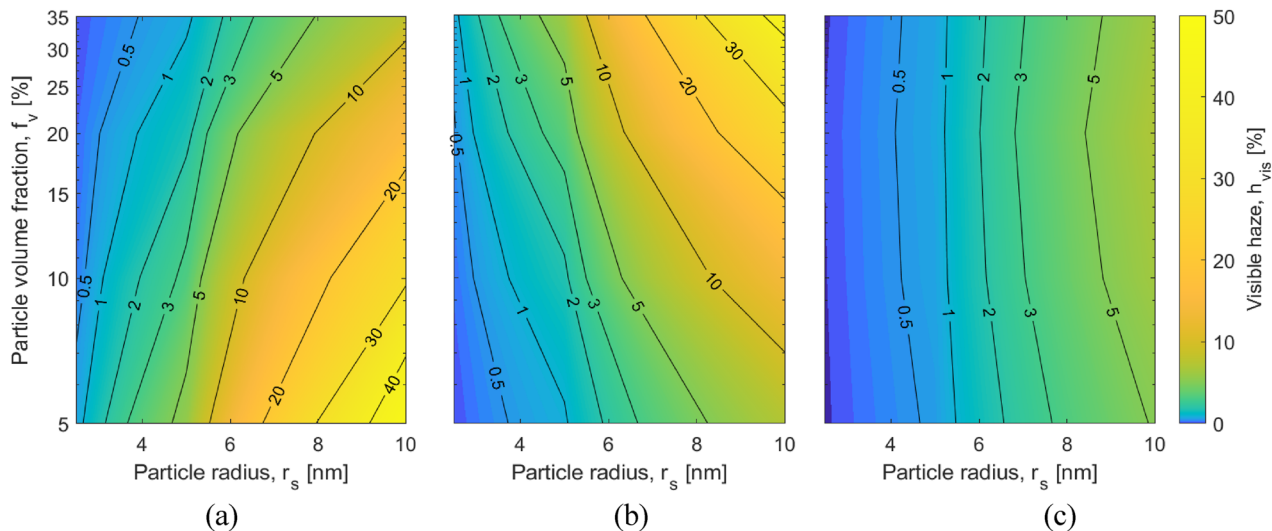


FIG. 7. (a) Numerical predictions of visible haze h_{vis} of 1-mm thick silica aerogel consisting of fractal aggregates of monodisperse particles as a function of particle radius r_s and volume fraction $f_v = 1 - \phi$. Corresponding visible haze h_{vis} of 1-mm thick suspensions of randomly distributed monodisperse particles predicted by (b) the Monte Carlo method assuming independent scattering and (c) the R^2T^2 method accounting for dependent scattering. In all cases, $L = 1$ mm, $n_{s,\lambda} = 1.5$, $k_{s,\lambda} = 0$, $n_{m,\lambda} = 1$, and $k_{m,\lambda} = 0$.³⁸

intensity $I_{\lambda,t}(\theta_t, \varphi_t)$ predicted by the R^2T^2 method as a function of particle radius r_s and volume fraction $f_v = 1 - \phi$ accounting for dependent scattering and for the complex aerogel microstructure. Figure 7 also shows the visible haze of a suspension of monodisperse particles randomly distributed in air obtained by (b) solving the RTE assuming independent scattering or (c) using the R^2T^2 method accounting for dependent scattering. Comparing Figs. 7(b) and 7(c) establishes that dependent scattering occurred in particle suspensions for all particle radii r_s between 3 and 10 nm and volume fractions $f_v \geq 5\%$. In fact, dependent scattering effects reduced the scattering and haze of the suspension compared to that predicted assuming independent scattering, as previously discussed.²⁶ Furthermore, comparing Figs. 7(a) and 7(c) establishes that the aggregation of the particles in the aerogel significantly increased haze. In other words, aerogel monoliths of fractally aggregated particles were more hazy than colloidal suspensions of randomly dispersed particles with the same thickness L , particle radius r_s , and porosity $\phi = 1 - f_v$. This can be attributed to the stronger scattering resulting from the aggregation of particles in secondary particles of larger characteristic length in the aerogel structures compared to particles of radius r_s .

F. Dependent scattering and fractal aggregation

Figure 8 illustrates the experimentally measured spectral normal-hemispherical transmittance $T_{nh,\lambda}$ as a function of wavelength λ ranging from 350 to 800 nm for the different silica aerogel monoliths synthesized and detailed in Table I with porosity (a) $\phi = 90.8\%$ (sample 1), (b) $\phi = 76.4\%$ (sample 2), and (c) $\phi = 47.6\%$ (sample 3). Figure 8 also illustrates the R^2T^2 method numerical predictions of spectral normal-hemispherical transmittance $T_{nh,\lambda}$ for the corresponding digital twins of samples 1–3 having the same porosity ϕ , monolith thickness L , and fractal dimension $D_f = 2.4$ consisting of polydisperse silica particles with average radius \bar{r}_s and standard deviation σ such that $\bar{r}_s \pm \sigma$ was 4.3 ± 1.0 nm, 4.3 ± 1.0 nm, and 8.9 ± 2.5 nm, respectively. Good agreement was obtained between the experimentally measured transmittance and that predicted by the R^2T^2 method accounting for both the aerogel microstructure and dependent scattering for all samples considered across the spectral window. Figure 8(d) also shows very good agreement between predictions and experimental measurements of the haze of sample 1. Note that the experimental measurements of haze for samples 2 and 3 were not reported due to a low signal-to-noise

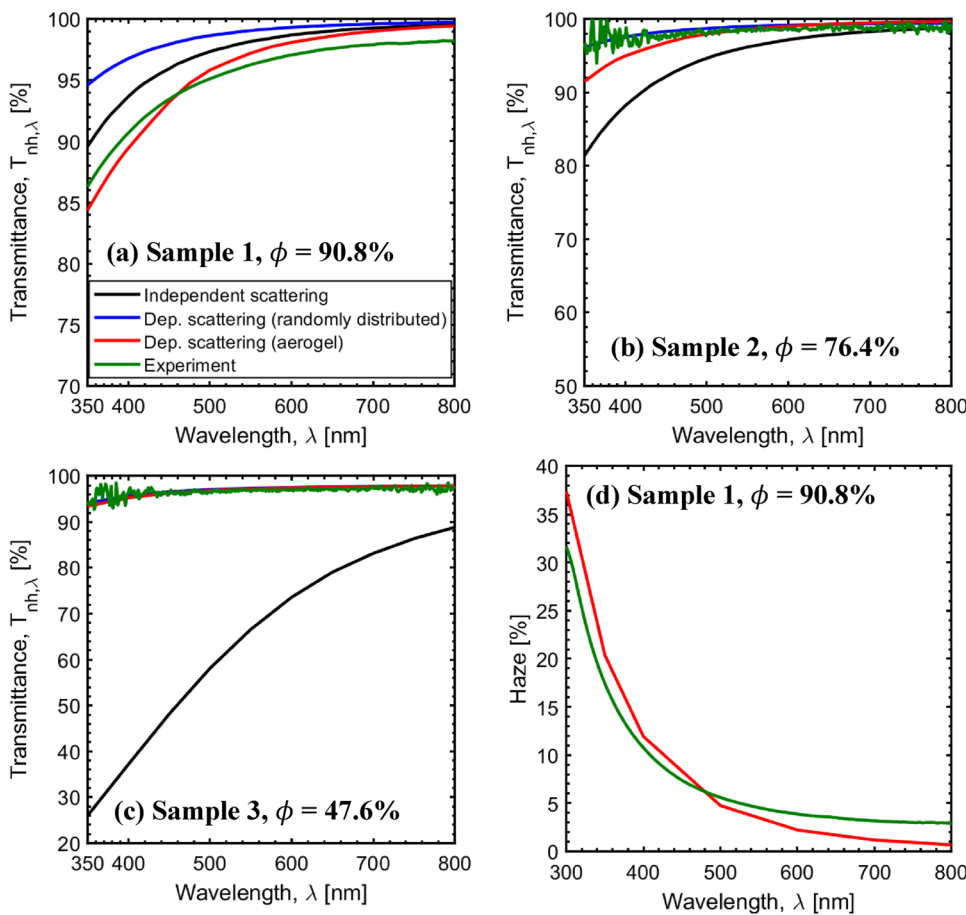


FIG. 8. Comparison of the spectral normal-hemispherical transmittance $T_{nh,\lambda}$ and spectral haze of aerogels (a) and (d) sample 1, (b) sample 2, and (c) sample 3 (Table I) measured experimentally and predicted by the R^2T^2 method for their respective digital twins along with the solutions of the RTE assuming independent scattering and of the R^2T^2 method accounting for dependent scattering but considering randomly distributed particles.

11 April 2025 22:30:34

ratio due to extremely low aerogel haze (<2%). Minor deviations between experimental measurements and numerical predictions by the R^2T^2 method may stem from the specific step length statistics applied in the Monte Carlo method, particularly near the aerogel boundaries.³⁹

Moreover, Figs. 8(a)–8(c) show the predictions of the transmittance $T_{nh,\lambda}$ assuming independent scattering or accounting for dependent scattering but for a suspension of randomly dispersed particles in air with the same particle size and volume fraction as samples 1, 2, or 3. However, these predictions deviated significantly from experimental measurements and numerical predictions by the R^2T^2 method for the computer-generated aerogels, particularly as the porosity increased. These results demonstrate that both dependent scattering, including both far-field and near-field effects,^{40–42} and particles' spatial arrangement play important roles in the interaction of aerogel slabs with electromagnetic waves. In fact, dependent scattering in aerogel monoliths reduces their transmittance at large porosities ($\phi \sim 90\%$) but increases their transmittance at smaller porosities.⁴³ For larger porosities (sample 1), the differences between experimentally measured and numerically predicted aerogel transmittance were attributed to the inability of the independent scattering approximation to model scattering due to the secondary particles formed by the aggregates. For lower porosities (samples 2 and 3), dependent scattering prevailed and the independent scattering approximation failed to accurately predict the scattering coefficient (see Fig. S7 of the [supplementary material](#)).²⁶ Interestingly, predictions accounting for dependent scattering in a suspension of randomly distributed particles showed very good agreement with those accounting for particle aggregation as well as with the experimental measurements for sample 3 with the lowest porosity ($\phi = 47.6\%$). This was because at small porosities and large particle volume fractions, the interparticle distance in randomly distributed particles is similar to that in the aggregated particles of aerogels. Figure S1 illustrates this convergence by plotting the mean minimum interparticle distance as a function of particle volume fraction f_v . In other words, at sufficiently low porosities (i.e., high particle volume fractions), particles can be treated as randomly distributed and the aerogel's fractal microstructure has little effect on its optical response. However, fractal microstructure must be accounted for to obtain accurate predictions of aerogel transmittance, especially at high porosities ϕ .

VI. CONCLUSION

This study established dependent scattering (near field and far field) among particles, fractal aggregation of particles into aerogel structures, and how their polydispersity plays essential roles in the interaction of aerogel monoliths with electromagnetic waves in the visible regime. Reducing porosity and ensuring a small (<4 nm) and narrow particle size distribution can increase the transparency of the aerogel slabs. This study also developed a novel powerful computational framework capable of (1) generating aerogel microstructures as fractal aggregates of polydisperse particles with a realistic microstructure resembling that of actual aerogel monoliths and (2) simulating electromagnetic wave transport through a complex heterogeneous microstructure much thicker than the radiation wavelength. As a result, mesoporous slabs and other nanocomposite materials no longer have to be treated as homogeneous with some

effective optical properties or radiation characteristics estimated based on the independent scattering approximation. Instead, their heterogeneous nature, complex microstructure, and far-field and near-field interactions among particles can be rigorously accounted for using the method reported in this study. These results can be used to design photonic metamaterials to achieve desired optical behavior.

SUPPLEMENTARY MATERIAL

The [supplementary material](#) provides the following figures offering insights into the structural and optical behaviors of aerogel monoliths: Figure S1 compares the mean minimum interparticle distance of aggregated and randomly dispersed nanoparticles. Figure S2 compares the pore size distributions of aerogel monoliths with different porosities (samples 1–3) measured experimentally and predicted numerically for the corresponding digital twins. The effect of primary particle polydispersity on the pore size distribution is also illustrated in Fig. S3. Figure S4 shows the scattering coefficient at 500 nm and the pore size distribution of an aerogel slab of porosity $\phi = 90.8\%$ and mean primary particle radius $r_s = 4.3$ nm as a function of cropped ensemble diameter D_e . They both converge for cropped ensemble diameters $D_e > 60$ nm. Figure S5 shows the predicted scattering coefficient at 500 nm for the 512 particle ensembles generated. Figures S6 and S7 show the numerical predictions of the spectral scattering coefficient and reflectance in the visible for aerogel monolith with different porosities.

ACKNOWLEDGMENTS

R.A.Y. acknowledges the financial support from the Fulbright Scholar Program. This work also used computational and storage services associated with the Hoffman2 Shared Cluster provided by the UCLA Institute for Digital Research and Education's Research Technology Group.

This research was supported in part by the Advanced Research Project Agency-Energy (ARPA-E) Single-Pane Highly Insulating Efficient Lucid Designs (SHIELD) program (ARPA-E Award No. DE-AR0000738) and by the National Science Foundation NRT-INFEWS: Integrated Urban Solutions for Food, Energy, and Water Management (Grant No. DGE-1735325).

AUTHOR DECLARATIONS

Conflict of Interest

The authors have no conflicts to disclose.

Author Contributions

Refet A. Yalcin: Conceptualization (equal); Data curation (equal); Formal analysis (equal); Funding acquisition (equal); Validation (equal); Writing – original draft (equal); Writing – review & editing (equal). **Patricia E. McNeil:** Resources (equal). **Abhinav Bhanawat:** Investigation (supporting); Resources (supporting); Writing – review & editing (supporting). **Ricardo Martinez:** Investigation (supporting); Resources (supporting); Writing – review & editing (supporting). **Glareh N. Kashanchi:** Resources (supporting). **Sarah H. Tolbert:** Funding acquisition (supporting);

Investigation (supporting); Supervision (supporting). **Bruce S. Dunn:** Funding acquisition (supporting); Investigation (supporting); Supervision (supporting). **Laurent Pilon:** Conceptualization (equal); Funding acquisition (equal); Methodology (equal); Supervision (equal); Writing – review & editing (equal).

DATA AVAILABILITY

The data that support the findings of this study are available from the corresponding author upon reasonable request.

REFERENCES

- M. Marszewski, S. C. King, Y. Yan, T. Galy, M. Li, A. Dashti *et al.*, “Thick transparent nanoparticle-based mesoporous silica monolithic slabs for thermally insulating window materials,” *ACS Appl. Nano Mater.* **2**, 4547–4555 (2019).
- D. M. Butts, P. E. McNeil, M. Marszewski, E. Lan, T. Galy, M. Li *et al.*, “Engineering mesoporous silica for superior optical and thermal properties,” *MRS Energy Sustainability* **7**, 39 (2020).
- R. Baetens, B. P. Jelle, and A. Gustavsen, “Aerogel insulation for building applications: A state-of-the-art review,” *Energy Build.* **43**, 761–769 (2011).
- E. Strobach, B. Bhatia, S. Yang, L. Zhao, and E. N. Wang, “High temperature annealing for structural optimization of silica aerogels in solar thermal applications,” *J. Non-Cryst. Solids* **462**, 72–77 (2017).
- L. Zhao, E. Strobach, B. Bhatia, S. Yang, A. Leroy, L. Zhang, and E. N. Wang, “Theoretical and experimental investigation of haze in transparent aerogels,” *Opt. Express* **27**, A39 (2019).
- T. Galy, D. Huang, and L. Pilon, “Revisiting independent versus dependent scattering regimes in suspensions or aggregates of spherical particles,” *J. Quant. Spectrosc. Radiat. Transfer* **246**, 106924 (2020).
- K. S. Yee and J. S. Chen, “The finite-difference time-domain (FDTD) and the finite-volume time-domain (FVTD) methods in solving Maxwell’s equations,” *IEEE Trans. Antennas Propag.* **45**, 354–363 (1997).
- B. T. Draine and P. J. Flatau, “Discrete-dipole approximation for scattering calculations,” *J. Opt. Soc. Am. A* **11**, 1491 (1994).
- P. Monk, *Finite Element Methods for Maxwell’s Equations* (Oxford University Press, 2007).
- D. W. Mackowski and M. I. Mishchenko, “A multiple sphere T-matrix Fortran code for use on parallel computer clusters,” *J. Quant. Spectrosc. Radiat. Transfer* **112**, 2182–2192 (2011).
- R. Tazaki, H. Tanaka, S. Okuzumi, A. Kataoka, and H. Nomura, “Light scattering by fractal dust aggregates. I. Angular dependence of scattering,” *Astrophys. J.* **823**, 70 (2016).
- J. M. Dlugach, M. I. Mishchenko, and D. W. Mackowski, “Numerical simulations of single and multiple scattering by fractal ice clusters,” *J. Quant. Spectrosc. Radiat. Transfer* **112**, 1864–1870 (2011).
- R. Ceolato, M. J. Berg, and N. Riviere, “Spectral and angular light-scattering from silica fractal aggregates,” *J. Quant. Spectrosc. Radiat. Transfer* **131**, 160–165 (2013).
- M. I. Mishchenko, “Poynting–Stokes tensor and radiative transfer in discrete random media: The microphysical paradigm,” *Opt. Express* **18**, 19770 (2010).
- M. F. Modest, *Radiative heat transfer* (Academic Press, 2013).
- G. Mie, “Beiträge zur Optik trüber Medien, speziell kolloidaler Metallösungen,” *Ann. Phys.* **330**, 377–445 (1908).
- C. L. Tien and B. L. Drolen, “Thermal radiation in particulate media with dependent and independent scattering,” *Annu. Rev. Heat Transfer* **1**, 1–32 (1987).
- M. Q. Brewster and C. L. Tien, “Radiative transfer in packed fluidized beds: Dependent versus independent scattering,” *J. Heat Transfer* **104**, 573–579 (1982).
- J. D. Cartigny, Y. Yamada, and C. L. Tien, “Radiative transfer with dependent scattering by particles: Part 1—Theoretical investigation,” *J. Heat Transfer* **108**, 608–613 (1986).
- Y. Yamada, J. D. Cartigny, and C. L. Tien, “Radiative transfer with dependent scattering by particles: Part 2—Experimental investigation,” *J. Heat Transfer* **108**, 614–618 (1986).
- B. L. Drolen and C. L. Tien, “Independent and dependent scattering in packed-sphere systems,” *J. Thermophys. Heat Transfer* **1**, 63–68 (1987).
- T. Galy and L. Pilon, “Dependent scattering effects in aggregates with touching or overlapping non-absorbing spherical particles,” *J. Quant. Spectrosc. Radiat. Transfer* **278**, 108018 (2022).
- M. I. Mishchenko, “Asymmetry parameters of the phase function for densely packed scattering grains,” *J. Quant. Spectrosc. Radiat. Transfer* **52**, 95–110 (1994).
- B. X. Wang and C. Y. Zhao, “Structural correlations and dependent scattering mechanism on the radiative properties of random media,” *J. Quant. Spectrosc. Radiat. Transfer* **218**, 72–85 (2018).
- L. Tsang and A. Ishimaru, “Radiative wave equations for vector electromagnetic propagation in dense nontenuous media,” *J. Electromagn. Waves Appl.* **1**, 59–72 (1987).
- R. A. Yalcin, T. Lee, G. N. Kashanchi, J. Markkanen, R. Martinez, S. H. Tolbert, and L. Pilon, “Dependent scattering in thick and concentrated colloidal suspensions,” *ACS Photonics* **9**, 3318–3332 (2022).
- K. Muinonen, J. Markkanen, T. Väisänen, J. Peltoniemi, and A. Penttilä, “Multiple scattering of light in discrete random media using incoherent interactions,” *Opt. Lett.* **43**, 683 (2018).
- T. Väisänen, J. Markkanen, A. Penttilä, and K. Muinonen, “Radiative transfer with reciprocal transactions: Numerical method and its implementation,” *PLoS One* **14**, e0210155 (2019).
- T. Galy, D. Mu, M. Marszewski, and L. Pilon, “Computer-generated mesoporous materials and associated structural characterization,” *Comput. Mater. Sci.* **157**, 156–167 (2019).
- J. Morán, J. Yon, A. Poux, F. Corbin, F.-X. Ouf, and A. Siméon, “Monte Carlo Aggregation Code (MCAC) Part 2: Application to soot agglomeration, highlighting the importance of primary particles,” *J. Colloid Interface Sci.* **575**, 274–285 (2020).
- R. A. Yalcin, CYAXARES: A python/MATLAB Package for the simulation of light transfer in particulate dense media using Monte Carlo method <https://github.com/refetaliyalcin/cyaxares> (accessed 22 May 2023).
- K. Sagawa and K. Takeichi, “Spectral luminous efficiency functions in the mesopic range,” *J. Opt. Soc. Am. A* **3**, 71 (1986).
- M. Marszewski, D. Butts, E. Lan, Y. Yan, S. C. King, P. E. McNeil *et al.*, “Effect of surface hydroxyl groups on heat capacity of mesoporous silica,” *Appl. Phys. Lett.* **112**, 201903 (2018).
- M. Jaroniec, “Evaluation of the fractal dimension from a single adsorption isotherm,” *Langmuir* **11**, 2316–2317 (1995).
- M. Woźniak, “Characterization of nanoparticle aggregates with light scattering techniques,” Aix-Marseille Université (2012).
- R. A. Yalcin, Aerogel structure database, https://github.com/refetaliyalcin/aerogel_structures (accessed 28 November 2024).
- J. Bertolotti, K. Vynck, L. Pattelli, P. Barthelemy, S. Lepri, and D. S. Wiersma, “Engineering disorder in superdiffusive Lévy glasses,” *Adv. Funct. Mater.* **20**, 965–968 (2010).
- R. A. Yalcin, P. E. McNeil, G. N. Kashanchi, R. Martinez, S. H. Tolbert, B. S. Dunn *et al.*, “Dependent scattering in silica ambigel monoliths—Experiments and simulations,” in *Proceeding of Proceedings of the 10th International Symposium on Radiative Transfer, RAD-23 Thessaloniki, Greece, 12–16 June 2023* (Begellhouse, Danbury, CT, 2023), pp. 211–218.
- F. Tommasi, L. Pattelli, S. Cavaliere, L. Fini, M. Paolucci, E. Pini *et al.*, “Anomalous radiative transfer in heterogeneous media,” *Adv. Theory Simul.* **7**, 2400182 (2024).
- R. Rezvani Naraghi, S. Sukhov, J. J. Sáenz, and A. Dogariu, “Near-field effects in mesoscopic light transport,” *Phys. Rev. Lett.* **115**, 203903 (2015).
- R. Martinez, A. Bhanawat, R. A. Yalcin, and L. Pilon, “Rigorous accounting for dependent scattering in thick and concentrated nanoemulsions,” *J. Phys. Chem. C* **128**, 6419–6430 (2024).
- A. Bhanawat, R. Martinez, R. A. Yalcin, T. Lee, and L. Pilon, “Dependent scattering and plasmon coupling in concentrated suspensions of optically hard nanoparticles,” *Appl. Phys. Lett.* **125** (2024).
- L. Pattelli, A. Egel, U. Lemmer, and D. S. Wiersma, “Role of packing density and spatial correlations in strongly scattering 3D systems,” *Optica* **5**, 1037 (2018).